The Freezing of Flexible Vesicles of Spherical Topology

G. Gompper, D. Kroll

The Freezing of Flexible Vesicles of Spherical Topology

G. Gompper ([1,*]) and D.M. Kroll ([2])

([1]) Max-Planck-Institut für Kolloid- und Grenzflächenforschung, Kantstrasse 55, 14513 Teltow, Germany
([2]) Department of Medicinal Chemistry and Minnesota Supercomputer Institute, University of Minnesota, 308 Harvard Street SE, Minneapolis, MN 55455, USA

(Received 20 March 1997, revised 19 June 1997, accepted 23 July 1997)

PACS.05.40.+j – Fluctuation phenomena, random processes, and Brownian motion
PACS.64.60.Fr – Equilibrium properties near critical points, critical exponents
PACS.87.22.Bt – Membranes and subcellular physics and structure

Abstract. — The freezing transition of tensionless fluctuating vesicles is investigated by Monte Carlo simulations and scaling arguments for a simple tether-and-bead model of fluid membranes. In this model, a freezing transition is induced by reducing the tether length. In the case of planar membranes (with periodic boundary conditions), the model shows a fluid-to-crystalline transition at a tether length $\ell_0 \simeq (1.53 \pm 0.01)\sigma_0$, where σ_0 is the bead diameter. For flexible vesicles with bending rigidities $0.85 k_B T \leq \kappa \leq \sqrt{3} k_B T$, the reduced free energy of dislocations with Burgers vector $\langle \ell \rangle$, $F_{\rm dloc}/\kappa$, is found to scale for small tether lengths with the scaling variable $\kappa/(K_0 \langle \ell \rangle^2)$, where K_0 is the Young modulus of a crystalline membrane of the same tether length, and $\langle \ell \rangle$ is the average nearest-neighbor distance. This is a strong indication that free dislocations are present, so that the membrane is in a hexatic phase for small tether lengths. A hexatic-to-fluid transition occurs with increasing tether length. With decreasing bending rigidity, this transition moves to smaller tether lengths.

1. Introduction

The melting transition of a planar two-dimensional membrane can be a two-step process which proceeds by a proliferation of topological defects [1–5]. At very low temperatures, dislocations are suppressed due to their cost in elastic stretching energy, which increases logarithmically with system size. The translational entropy of a dislocation shows the same size dependence as the stretching energy, so that the free energy of dislocations decreases with increasing temperature. At a temperature T_1, free dislocations appear and destroy the quasi-long-ranged translational order of the crystal; this leads to a hexatic phase, which still retains quasi-long-ranged bond orientational order. At a higher temperature T_2, disclinations proliferate, causing a transition to a fluid phase characterized by short-ranged translational and bond-orientational correlations. It is also possible that a first-order transition takes the crystal directly into a fluid phase [5,6].

This scenario changes when the membrane is flexible [7–9], so that it can buckle out of plane. The free energy of a defect is now determined by the balance of stretching and bending energies [8, 10, 11]. A $T = 0$ analysis of defect shapes by Seung and Nelson [11] shows that the elastic energy of dislocations is so reduced by buckling that these defects destroy

(*) Author for correspondence (e-mail: gompper@mpikg-teltow.mpg.de)

the crystalline order at any finite temperature. A flexible membrane is therefore expected to have a Kosterlitz-Thouless (KT) transition from a low-temperature hexatic to a high-temperature fluid phase [12, 13]. The transition temperature is predicted to decrease with decreasing bending rigidity [13].

The unusual properties of a hexatic membrane have interesting consequences for the shape of both vesicles [14,15] and open membranes with isolated disclinations [16,17]. In particular, it has been shown that vesicles of genus zero have a non-spherical equilibrium shape which resembles an icosahedron with smooth edges [15].

There have recently been a number of extensive simulation studies of triangulated surfaces using both fixed and dynamic triangulations with the goal of determining the properties of crystalline (or polymerized) and fluid membranes, respectively. It is therefore natural to consider the transition between these two classes of membranes using a triangulated surface model that contains a parameter which tunes the density of ($q = 6$)-fold-coordinated vertices. This has been done in reference [18] using a model of self-intersecting random surfaces with the Hamiltonian

$$\mathcal{H} = \frac{1}{2}\sum_{\langle ij\rangle}(\mathbf{r}_i - \mathbf{r}_j)^2 + \gamma\sum_i |q_i - 6|^m, \tag{1}$$

where q_i is the coordination number, and $\mathbf{r}_i$ the position, of vertex i. The first sum runs over all nearest-neighbor pairs of vertices, and the second over all vertices. Note that this model does not contain a bending elasticity. It is argued in reference [18] that terms with $m \geq 2$ correspond to higher-order curvature contributions, and should thus be irrelevant for the behavior on long length scales. For $m = 1$, the in-plane geometry is found to get regularized with increasing γ, *i.e.* the number of vertices with coordination number not equal to six decreases. However, the effect on the external geometry, *i.e.* on the radius of gyration, was found to be very weak.

Another model for the freezing of self-intersecting random surfaces was suggested in reference [19]. In this case, a term is added to the Hamiltonian which is proportional to the distance of the triangulation $\mathcal{T}$ from some reference triangulation $\mathcal{T}_0$. This distance is defined as the minimum number of bond flips [20, 21] necessary to change $\mathcal{T}$ into $\mathcal{T}_0$. This model is clearly rather difficult to investigate, and has as yet not been studied for any finite-dimensional embedding space. Furthermore, as a model for lipid bilayer membranes, it is unclear how such a — highly non-local — contribution to the energy would arise from microscopic interactions.

In this paper, we present the results of a simulation study of the freezing of low-bending-rigidity membranes. We employ a simple tether-and-bead model of self-avoiding fluid membranes [22, 23] which has been used previously to study the phase diagram and scaling behavior of fluid vesicles as a function of the bending rigidity and a trans-membrane pressure increment [22–30], the renormalization of the bending rigidity [30–32], the shape of vesicles in elongational flow [33], and the driven transport of vesicles through narrow pores [34]. In this model, crystalline order is induced by reducing the tether length. The tethering constraint acts like an attractive interaction between neighboring beads; the reduction of the tether length is thus very much like the increase of the strength of an attractive interaction in a molecular model. The tether-and-bead model is the simplest model for simulation studies of the freezing of flexible membranes since it contains only two parameters, the bending rigidity λ_b, which controls the out-of-plane fluctuations, and the tether length ℓ_0, which controls the in-plane density and, more importantly, the in-plane shear modulus. This is the minimal number of parameters required. Similar models have been employed to study the equilibrium behavior [35] and the phase separation dynamics [36,37] of two-component fluids in two dimensions — which corresponds to planar two-component membranes.

Part of the results described in this paper have been summarized elsewhere [38].

2. Tether-and-Bead Model

Our model [22, 23] of fluid membranes consists of N hard spheres of diameter $\sigma_0 = 1$ which are connected by tethers of maximum extension $\ell_0 < \sqrt{3}\sigma_0$ to form a triangular network of spherical topology. In order to allow for diffusion within the membrane, tethers can be cut and reattached between the four beads which form two neighboring triangles [20, 21]. A Monte Carlo step then consists of a random displacement of all beads in the cube $[-s, s]^3$, followed by N attempted tether cuts. The step size s is chosen such that approximately 50% of the attempted bead moves are accepted. We use the discretization [39]

$$E_{\mathrm{b}} = \lambda_{\mathrm{b}} \sum_{\langle ij \rangle} (1 - \mathbf{n}_i \cdot \mathbf{n}_j), \tag{2}$$

for the curvature energy, where the sum runs over all pairs of neighboring triangles, and $\mathbf{n}_i$ is the surface normal vector of triangle i. The parameter λ_{b} in equation (2) is related to the bending rigidity κ of the continuum curvature model [32] by $\kappa = \lambda_{\mathrm{b}}/\sqrt{3}$. We have studied both vesicles with finite κ as well as planar membranes ($\kappa \to \infty$) with periodic boundary conditions. In the former case, two systems sizes, $N = 247$ and $N = 407$, were used, and averages were taken over runs of up to 500 million Monte Carlo steps (per vertex). In the latter case, system sizes $N = 100$, $N = 196$, $N = 400$ and $N = 800$ were studied, with runs of up to 200 million Monte Carlo steps.

3. Planar Membranes

3.1. Monte Carlo Method. — In two dimensions, we have performed simulations of tensionless networks with periodic boundary conditions. We use a scheme in which both the size and the shape of the simulation cell fluctuates — this allowed us to determine both Lamé constants in the solid phase — as well as a scheme with fluctuating area but fixed cell shape — which is more stable close to the crystalline-to-fluid transition.

In order to perform simulations at constant tension σ, both the lengths and orientations of the cell basis vectors are allowed to fluctuate. The simulation procedure we utilize is based on the isothermal-isobaric Monte Carlo methods introduced by McDonald [40] and subsequently generalized by Yashonath and Rao [41]. The simulation cell shape is described by the matrix $\mathbf{h} = (\mathbf{a}, \mathbf{b})$ of the two vectors $\mathbf{a}$ and $\mathbf{b}$ that span the simulation cell. The position of a particle in the cell is

$$\mathbf{r}_i = \mathbf{h}\mathbf{s}_i = \xi_i \mathbf{a} + \eta_i \mathbf{b}, \tag{3}$$

where $\mathbf{s}_i = (\xi_i, \eta_i)^T$, with $0 \leq \xi_i, \eta_i \leq 1$. The simulation is performed in the scaled coordinate $\{\mathbf{s}_i\}$. A Monte Carlo step then consists of a random displacement of all beads in the square $[-\delta, \delta]^2$ followed by N attempted tether cuts. The step size δ is again chosen such that approximately 50% of the attempted bead moves are accepted. Every five sweeps, the independent elements of the matrix $\mathbf{h}$ are updated using a standard Metropolis algorithm with the weight $\exp(-\delta H_{\mathrm{on}})$, where [40–42]

$$\delta H_{\mathrm{on}} = \delta V_{\mathrm{on}} + \sigma(A_{\mathrm{n}} - A_{\mathrm{o}}) - N \ln(A_{\mathrm{n}}/A_{\mathrm{o}}). \tag{4}$$

The area A is given by $A = \det\{\mathbf{h}\}$, and the subscripts o and n refer to the old and new states, respectively. δV_{on} is the total change in interaction potential on going from state o to n. Because of the hard-sphere nature of the beads and the fixed tether lengths, it is either zero or infinite, depending upon whether or not the cell update leads to bead overlap or neighbor

distances which exceed the tether length. The last term in equation (4) arises from the Jacobi determinant of the transformation (3). Moves are then accepted with a probability equal to $\min(1, \exp[-\delta H_{\rm on}])$ [42].

If the shape of the simulation cell is kept fixed, only the area fluctuates, and equation (4) is used to determine the probability that an area update is accepted. In the case of fluctuating cell shape, the most general parameterization of the cell is $\mathbf{a} = (a_1, a_2)$, $\mathbf{b} = (b_1, c_1)$. We choose the vector $\mathbf{a}$ to point in the x-direction, *i.e.* we set $a_2 \equiv 0$. This choice breaks the rotational symmetry of the whole system, and requires an additional Faddeev-Popov term [43] in the weight $\exp(-\delta H_{\rm on})$, which now reads

$$\delta H_{\rm on} = \delta V_{\rm on} + \sigma(A_{\rm n} - A_{\rm o}) - N \ln(A_{\rm n}/A_{\rm o}) - \ln(a_{1\rm n}/a_{1\rm o}). \tag{5}$$

By treating the three parameters (a_1, b_1, c_1) as dynamical variables, the length of both sides as well as the inner angle of the simulation cell fluctuate independently. Our initial configuration is an $L \times L = N$ triangular array of beads. Periodic boundary conditions were used in order to minimize boundary effects.

3.2. Elastic Constants. — The elastic constants can be expressed in terms of correlations of the strain tensor [44,45]

$$\boldsymbol{\epsilon} = \frac{1}{2}\left[(\mathbf{h}_0^T)^{-1}\mathbf{G}\,\mathbf{h}_0^{-1} - \mathbf{1}\right], \tag{6}$$

where $\mathbf{1}$ is the unit matrix and the matrix of reference basis vectors $\mathbf{h}_0$ is determined by the requirement $\langle\boldsymbol{\epsilon}\rangle = 0$. The metric tensor is $\mathbf{G} = \mathbf{h}^T\mathbf{h}$. In particular,

$$\mathcal{A}\langle\epsilon_{ij}\epsilon_{kl}\rangle = k_{\rm B}T S_{ijkl}, \tag{7}$$

where $\mathcal{A}$ is the area of the network and the elastic compliance tensor

$$S_{ijkl} = -\frac{\lambda}{4\mu(\mu+\lambda)}\delta_{ij}\delta_{kl} + \frac{1}{4\mu}(\delta_{ik}\delta_{jl} + \delta_{il}\delta_{jk}), \tag{8}$$

where λ and μ are the two-dimensional Lamé coefficients. Using equations (7, 8), one finds that

$$\langle\epsilon_{11}\epsilon_{22}\rangle = -\frac{k_{\rm B}T}{\langle A\rangle}\frac{\lambda}{4\mu(\lambda+\mu)}, \tag{9}$$

$$\langle\epsilon_{12}\epsilon_{12}\rangle = \frac{k_{\rm B}T}{\langle A\rangle}\frac{1}{4\mu}, \tag{10}$$

and

$$\langle\epsilon_{11}\epsilon_{11}\rangle = \langle\epsilon_{22}\epsilon_{22}\rangle = \frac{k_{\rm B}T}{\langle A\rangle}\frac{\lambda+2\mu}{4\mu(\lambda+\mu)} \equiv \frac{k_{\rm B}T}{\langle A\rangle\, K_0}, \tag{11}$$

where $\langle A\rangle = \det\{\mathbf{h}_0\}$, and K_0 is the Young modulus.

These results can be used to determine the area compressibility

$$k_{\rm B}T\,K_{\rm A} = \frac{k_{\rm B}T}{\lambda+\mu} = \langle A\rangle\langle(\epsilon_{11}+\epsilon_{22})^2\rangle \tag{12}$$

and the Poisson ratio

$$\sigma_{\rm P} = \frac{\lambda}{(\lambda+2\mu)} = -\frac{\langle\epsilon_{11}\epsilon_{22}\rangle}{\langle\epsilon_{11}\epsilon_{11}\rangle} = 1 - \frac{1}{2}K_0K_{\rm A}. \tag{13}$$

Equation (12) is the linear-response approximation to the exact area compressibility

$$k_{\mathrm{B}}T\,K_{\mathrm{A}} = (\langle A^2\rangle - \langle A\rangle^2)/\langle A\rangle. \tag{14}$$

In the crystalline phase, these two expressions are equivalent in the thermodynamic limit. However, in a finite system, the last equality in equation (13) only holds when the linear-response result (12) is used.

In order to determine the strain correlation functions, it is convenient to express the elements of the strain tensor in terms of the basis vectors $\{\mathbf{a},\mathbf{b}\}$ of the simulation cell. Choosing the 1-axis to coincide with the direction of $\mathbf{a}$, one finds

$$\epsilon_{11} = (\mathbf{a}^2/c^2 - 1)/2, \tag{15}$$

$$\epsilon_{12} = \epsilon_{21} = \mathbf{a}\cdot\mathbf{g}/(2c^2), \tag{16}$$

and

$$\epsilon_{22} = (\mathbf{g}^2/c^2 - 1)/2, \tag{17}$$

where $\mathbf{g} \equiv (2\mathbf{b} - \mathbf{a})/\sqrt{3}$. The equilibrium length, c, of the cell edge is defined by the thermal averages $c^2 \equiv \langle\mathbf{a}^2\rangle = \langle\mathbf{b}^2\rangle = \langle\mathbf{g}^2\rangle$, and the angle between the average directions of the two basis vectors is $\pi/3$. We have checked explicitly that $\langle\mathbf{a}\cdot\mathbf{g}\rangle$ converges to zero in our simulations of the crystalline phase.

In order to simplify our notation, we will set $k_{\mathrm{B}} = 1$ in the following, *i.e.* the temperature T will be given in energy units.

3.3. Mean-Field Approximation. — In order to gain some insight into the dependence of the elastic properties of our tether-and-bead model on the tether length ℓ_0, we employ a simple mean-field approximation in which correlations between neighboring triangles are ignored [46]. The elastic moduli can then be obtained by studying the shape fluctuations of a single triangle. We fix one corner of the triangle at the origin. Let $\mathbf{s}_1$ and $\mathbf{s}_2$ be the position vectors of the other two beads, and ϕ the angle between them. The hard-core repulsion and the tethering potential restrict the lengths of the bond vectors to lie in the range $1 \le s_1 \le \ell_0$ and $1 \le s_2 \le \ell_0$, and $\phi_{\min} \le \phi \le \phi_{\max}$, with

$$\phi_{\min} = \arccos\left[(s_1^2 + s_2^2 - 1)/(2s_1s_2)\right] \tag{18}$$

$$\phi_{\max} = \arccos\left[(s_1^2 + s_2^2 - \ell_0^2)/(2s_1s_2)\right]. \tag{19}$$

Averages of some quantity $Q(s_1, s_2, \phi)$ are then given by [47]

$$\langle Q\rangle = \frac{1}{Z}\,2\pi\cdot\int_1^{\ell_0} \mathrm{d}s_1 s_1 \int_1^{\ell_0} \mathrm{d}s_2 s_2 \int_{\phi_{\min}}^{\phi_{\max}} \mathrm{d}\phi\; Q(s_1, s_2, \phi), \tag{20}$$

where

$$Z = 2\pi \int_1^{\ell_0} \mathrm{d}s_1 s_1 \int_1^{\ell_0} \mathrm{d}s_2 s_2 \int_{\phi_{\min}}^{\phi_{\max}} \mathrm{d}\phi\; 1 \tag{21}$$

is the partition function.

Using equations (11, 12, 13) of the previous section, we can now easily calculate the elastic moduli K_{A}, K_0 and the Poisson ratio σ_{P}. The numerical data in the range $1 < \ell_0 < 1.6$ are

very well fitted by the expressions

$$\sigma_{\rm P} = \frac{1}{3} + \frac{1}{5}\left(\frac{\ell_0 - 1}{\ell_0 + 1}\right)^2 \tag{22}$$

$$T K_{\rm A} = \frac{1}{20.785}(\ell_0 - 1)^2 \left[1 - 1.53\left(\frac{\ell_0 - 1}{\ell_0 + 1}\right)^2\right] \tag{23}$$

$$K_0/T = 27.713(\ell_0 - 1)^{-2}\left[1 + 1.23\left(\frac{\ell_0 - 1}{\ell_0 + 1}\right)^2\right]. \tag{24}$$

The dimensionless ratio $(\ell_0 - 1)/(\ell_0 + 1)$ appears naturally since the average bond length is very well approximated by $\langle \ell \rangle \simeq (1+\ell_0)/2$. Note that the mean-field results satisfy the relation $\sigma_{\rm P} = 1 - K_0 K_{\rm A}/2$ exactly.

3.4. Monte Carlo Results. — For a tensionless membrane, the density is determined by the tether length ℓ_0. It is easy to see that for $\ell_0 \leq \sqrt{2}$, steric constraints make bond flips impossible; a glass transition therefore occurs at this value of ℓ_0. Our simulations indicate that the solid phase remains stable as the tether length in increased, until at $\ell_0 = 1.53 \pm 0.01$ there is a melting transition.

In the crystalline phase, our Monte Carlo data for the area compressibility (see Fig. 5 below) and for the Young modulus are well fitted by the expressions

$$T K_{\rm A} = \frac{1}{8.5}(\ell_0 - 1)^2 \left[1 + 1.8\left(\frac{\ell_0 - 1}{\ell_0 + 1}\right)^2\right] \tag{25}$$

$$K_0/T = 11.33(\ell_0 - 1)^{-2}\left[1 - 2.1\left(\frac{\ell_0 - 1}{\ell_0 + 1}\right)^2\right]. \tag{26}$$

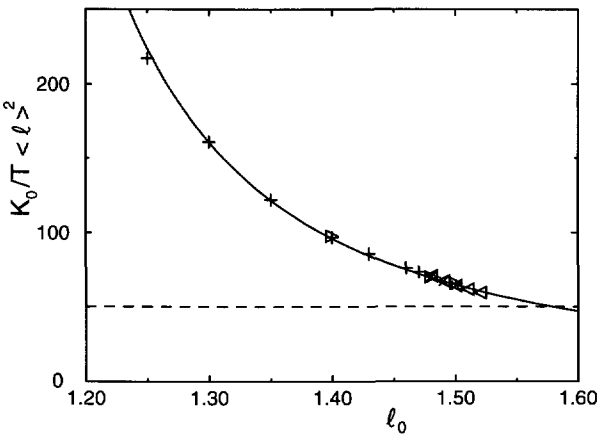

Fig. 1. — Dimensionless Young modulus $\bar{K}_0 = (K_0/T)\langle \ell \rangle^2$ for flat membranes as a function of the tether length ℓ_0. Monte Carlo data are shown for $N = 100$ (+), $N = 196$ (×), and $N = 400$ (◁, ▷). The solid line shows the fit (26). The dashed line is the stability limit ($\bar{K}_0 = 16\pi$) predicted by the KTHNY-theory.

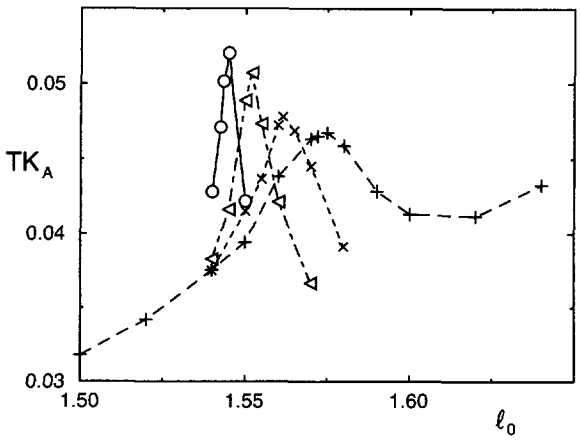

Fig. 2. — Area compressibility TK_A for flat membranes as a function of the tether length ℓ_0. Monte Carlo data are shown for $N = 100$ (+), $N = 196$ (×), $N = 400$ (◁) and $N = 800$ (○). The lines are guides to the eye.

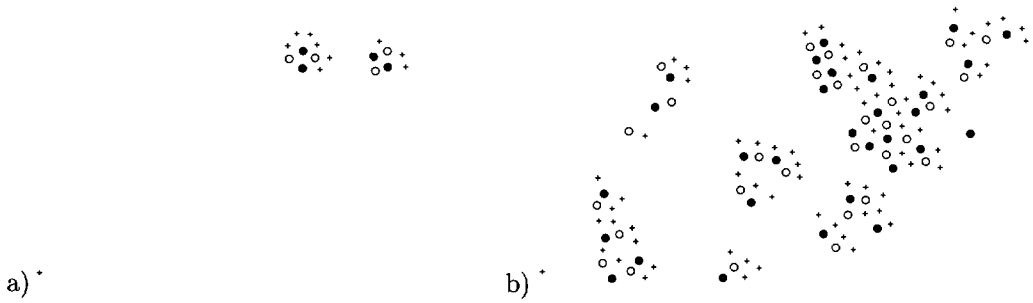

Fig. 3. — Typical configurations of planar, two-dimensional membranes of $N = 400$ beads near the fluid-to-crystalline transition, with (a) $\ell_0 = 1.53$, and (b) $\ell_0 = 1.55$. Fivefold (sevenfold) disclinations are shown by open (full) circles, sixfold-coordinated vertices by crosses.

The dimensionless Young modulus, $\bar{K}_0 = (K_0/T)\langle\ell\rangle^2$, is shown in Figure 1. Note that $\bar{K}_0$ given by equation (26) reaches the stability limit of the crystalline phase predicted by the KTHNY-theory [1–4], $\bar{K}_0 = 16\pi$, at $\ell_0 = 1.579$. The area compressibility (see Eq. (14)) determined in simulations with a fixed cell shape is shown in Figure 2. Note that the maximum of K_A moves to smaller tether lengths with increasing system size, so that $\ell_0 = 1.545$ — the peak position for $N = 800$ — is an upper limit for the transition point. The critical tether length, $\ell_0^c = 1.53 \pm 0.01$, which we obtain from an extrapolation (to infinite system size) of the peak position of the area compressibility, is therefore considerably lower than this stability limit, implying that the transition is first order. In contrast, the stability limit of the two-dimensional hard-sphere solid has been found to be extremely close to the melting transition [48]. Two typical configurations of the two-dimensional membrane near the transition are shown in Figures 3.

Our Monte Carlo results for the Poisson ratio for tether lengths in the interval $1.40 \leq \ell_0 \leq 1.50$ all fall in the range $\sigma_P = 0.34 \pm 0.02$, with a weak tendency towards larger values with increasing ℓ_0. The Monte Carlo data are therefore consistent with the mean-field expression

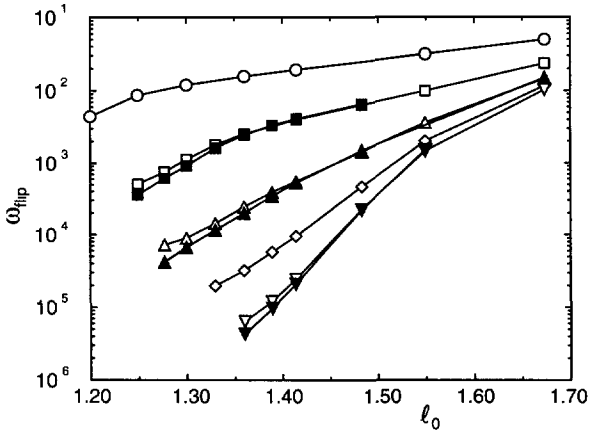

Fig. 4. — Bond-flip acceptance rate ω_{flip} of flexible vesicles as a function of the tether length ℓ_0. Monte Carlo data are shown for $N = 247$ with $\lambda_b/T = 1.0$ (○), $\lambda_b/T = 1.5$ (□), $\lambda_b/T = 2.0$ (△), $\lambda_b/T = 2.5$ (◇), and $\lambda_b/T = 3.0$ (▽), and for $N = 407$ with $\lambda_b/T = 1.5$ (■), $\lambda_b/T = 2.0$ (▲), and $\lambda_b/T = 3.0$ (▼).

(22). This agreement is quite reasonable, in particular since the numerical values of the amplitudes in the expressions for K_0 (compare Eqs. (24, 26)) and K_A (compare Eqs. (23, 25)) typically differ by factors of order 2, and the higher-order terms in $(\ell_0 - 1)^2$ even have different signs.

It is interesting to compare these results for the freezing transition of the tether-and-bead model with the freezing parameters of the two-dimensional hard-sphere fluid. The latter melts at an average density $\rho \simeq 0.90$, or an average nearest-neighbor distance $\langle \ell \rangle \simeq 1.13$ [49–51] (which corresponds to $\ell_0 \simeq 1.26$ in our tethered system). Since density fluctuations are suppressed by the tethering potential, the tethered fluid should indeed be expected to freeze at a lower density.

4. Fluctuating Vesicles

4.1. Internal Properties of Fluctuating Membranes. — For vesicles with finite κ/T, bond flips occur for any tether length with some (possibly very small) probability. We have monitored the bond-flip acceptance rate ω_{flip} in our runs. The result shown in Figure 4 is a smooth ℓ_0-dependence for all bending rigidities ($\kappa/T \leq \sqrt{3}$) studied. A glass transition therefore does not occur when the membrane is allowed to buckle out of plane. The acceptance rate varies roughly exponentially with ℓ_0 in the regime of the smallest tether lengths we are able to simulate and reach thermal equilibrium. The exponential behavior has to break down at very small tether lengths, since $\omega_{flip} \to 0$ for $\ell_0 \to 1^+$ In the limit of $\lambda_b/T \to \infty$, ω_{flip} must already vanish for $\ell_0 \to \sqrt{2}^+$

With increasing λ_b/T, the flip acceptance rate begins to deviate from the exponential behavior at $\ell_0 \simeq 1.33$ for $\lambda_b/T = 1.5$, $\ell_0 \simeq 1.41$ for $\lambda_b/T = 2.0$, $\ell_0 \simeq 1.55$ for $\lambda_b/T = 2.5$, and $\ell_0 \simeq 1.55$ for $\lambda_b/T = 3.0$. This change in the behavior of ω_{flip} yields a first indication of a phase transition from a hexatic or crystalline phase at small tether lengths to a fluid phase at larger tether lengths. The data show that with decreasing bending rigidity, this transition occurs at smaller and smaller tether lengths.

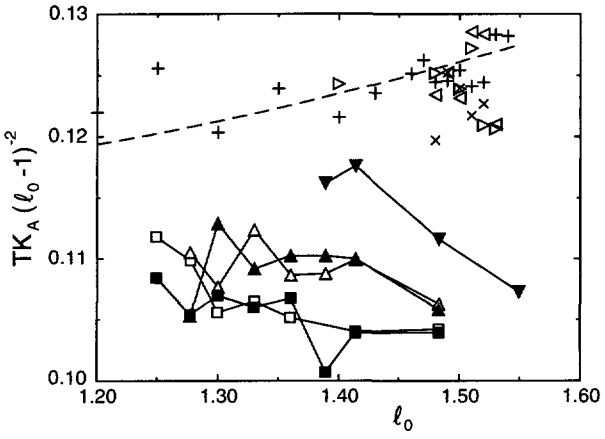

Fig. 5. — Scaled area compressibility $T K_A(\ell_0 - 1)^{-2}$, with $T K_A = (\langle A^2\rangle - \langle A\rangle^2)/\langle A\rangle$, of flexible vesicles and flat membranes as a function of the tether length ℓ_0. The symbols denote the same system sizes and bending rigidities as in Figure 4 for vesicles, and the same system sizes as in Figure 1 for planar membranes. The dashed line shows the fit (25).

The compressibility K_A of the internal area of fluctuating vesicles is shown in Figure 5 in scaled form, together with our data for planar membranes. The curves show that the amplitude of area fluctuations slowly decreases with decreasing bending rigidity. The effect becomes more pronounced for larger tether lengths. Thus, the area fluctuations of a flexible membrane are smaller than in the planar case, a result which is difficult to understand intuitively. Since the difference between the values of K_A which were measured for vesicles and planar membranes never exceeds 20% for the range of bending rigidities and tether lengths studied, it seem justified to use expression (25) for the area compressibility and (26) for the Young modulus for flexible vesicles.

The area compressibility is closely related to the average nearest-neighbor distance, $\langle \ell \rangle$, and its fluctuations. We find in our simulations that $\langle \ell \rangle$ can be very well approximated by $\langle \ell \rangle \simeq (1 + \ell_0)/2 \equiv \bar{\ell}$. The deviation, $\delta\ell = \langle \ell \rangle - \bar{\ell}$ is shown in Figure 6; it is less than 0.3% for all tether lengths studied. However, the excess nearest-neighbor distance shows a remarkable structure; for $\lambda_b/T \geq 1.5$, $\delta\ell$ has a pronounced peak. The position of this peak is $\ell_0 \simeq 1.30$ for $\lambda_b/T = 1.5$, $\ell_0 \simeq 1.36$ for $\lambda_b/T = 2.0$, $\ell_0 \simeq 1.39$ for $\lambda_b/T = 2.5$, and $\ell_0 \simeq 1.40$ for $\lambda_b/T = 3.0$. No peak is found for $\lambda_b/T = 1.0$. The reason for this difference is that fluid vesicles of the sizes studied are in the branched-polymer phase for $\lambda_b/T = 1.0$, whereas they are in an "extended" phase for values of the bending rigidity $\lambda_b/T \geq 1.25$ [30] for all tether lengths.

The change in behavior of ω_{flip} and the peak position of the excess nearest-neighbor distance $\delta\ell$ will be used in Section 4.6 below — together with several other quantities — to determine the phase diagram of flexible vesicles.

4.2. VESICLE SHAPES. — Several vesicle configurations for bending rigidity $\lambda_b/T = 2.0$ and various tether lengths are shown in Figures 7.

In order to characterize the vesicle shapes and shape fluctuations, we have determined the average volume $\langle V \rangle$, the compressibility

$$\chi = (\langle V^2\rangle - \langle V\rangle^2)/\langle V\rangle, \tag{27}$$

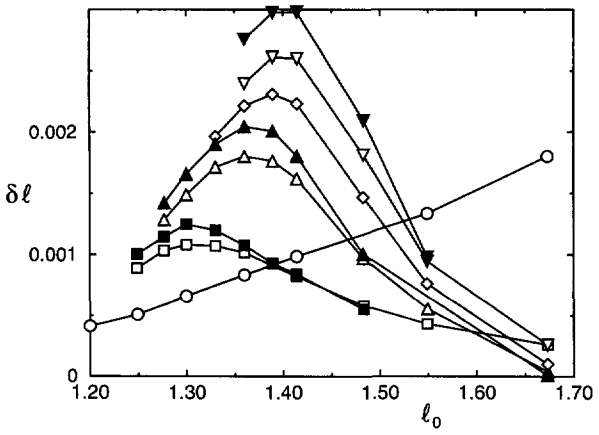

Fig. 6. — Excess nearest-neighbor distance, $\delta\ell = \langle\ell\rangle - (1+\ell_0)/2$, as a function of the tether length ℓ_0. Monte Carlo data are shown for $N = 247$ with $\lambda_b/T = 1.0$ (○), $\lambda_b/T = 1.5$ (□), $\lambda_b/T = 2.0$ (△), $\lambda_b/T = 2.5$ (◇), and $\lambda_b/T = 3.0$ (▽), and for $N = 407$ with $\lambda_b/T = 1.5$ (■), $\lambda_b/T = 2.0$ (▲), and $\lambda_b/T = 3.0$ (▼).

and the asphericity

$$\Delta_3 = \frac{\langle(\Lambda_1^2 + \Lambda_2^2 + \Lambda_3^2) - (\Lambda_1\Lambda_2 + \Lambda_2\Lambda_3 + \Lambda_3\Lambda_1)\rangle}{\langle(\Lambda_1 + \Lambda_2 + \Lambda_3)^2\rangle}, \tag{28}$$

where $\Lambda_1 < \Lambda_2 < \Lambda_3$ are the eigenvalues of the moments-of-inertia tensor. The asphericity varies in the range $0 \leq \Delta_3 \leq 1$, with $\Delta_3 = 0$ for spheres, and $\Delta_3 = 1$ in the limit of very elongated objects.

The coupling between vesicle shapes and in-plane defect structure is most pronounced for small bending rigidities, since a hexatic (self-avoiding) membrane should be in a smooth "crinkled" phase [12,13,52] (with an algebraic decay of the correlation function of surface normals), while a fluid membrane is crumpled at sufficiently large length scales [32,53–55]. On the other hand, a vesicle with a large bending rigidity is essentially spherical, independent of the internal state of the membrane. This behavior is indeed observed in the simulations. With decreasing tether length (at fixed λ_b/T of order unity) the vesicle becomes more spherical. This can be seen in the increase of the scaled volume $v \equiv \langle V\rangle N^{-3/2}\langle\ell\rangle^{-3}$, which is shown in Figure 8. Note that for a perfect sphere (of equilateral triangles of side length $\langle\ell\rangle$), $v = 2^{-5/2}3^{-1/4}\pi^{-1/2} = 0.0758$, and for a perfect icosahedron, $v = 2^{-9/2}3^{-1}5^{-1/2}(\sqrt{5}+1)^2 = 0.0690$. Thus, the vesicles with the largest bending rigidity or smallest tether length still deviate appreciably from a sphere, and, in fact, seem to have a reduced volume closer to that of an icosahedron than of a sphere. This is qualitatively consistent with the mean-field shapes calculated in reference [15]. In the fluid phase, larger vesicles have a smaller reduced volume due to increased thermal shape fluctuations [32].

The evolution of the vesicle shape with decreasing tether length can also be seen in the decrease of the volume compressibility [38] and of Δ_3, see Figure 9. The behavior of Δ_3 deserves some further discussion. A strong decrease with decreasing ℓ_0 is observed for $\lambda_b/T = 1.0$ and $\lambda_b/T = 1.5$. However, for $\lambda_b/T \geq 2.0$, the value of Δ_3 depends only very weakly on the tether length. This can also be seen in the probability distributions $P_i(\Gamma_i)$ of the ratios $\Gamma_i \equiv \Lambda_i/\Lambda_3$ (with $i = 1, 2$) of the eigenvalues of the moments-of-inertia tensor. The peak positions of $P_i(\Gamma_i)$

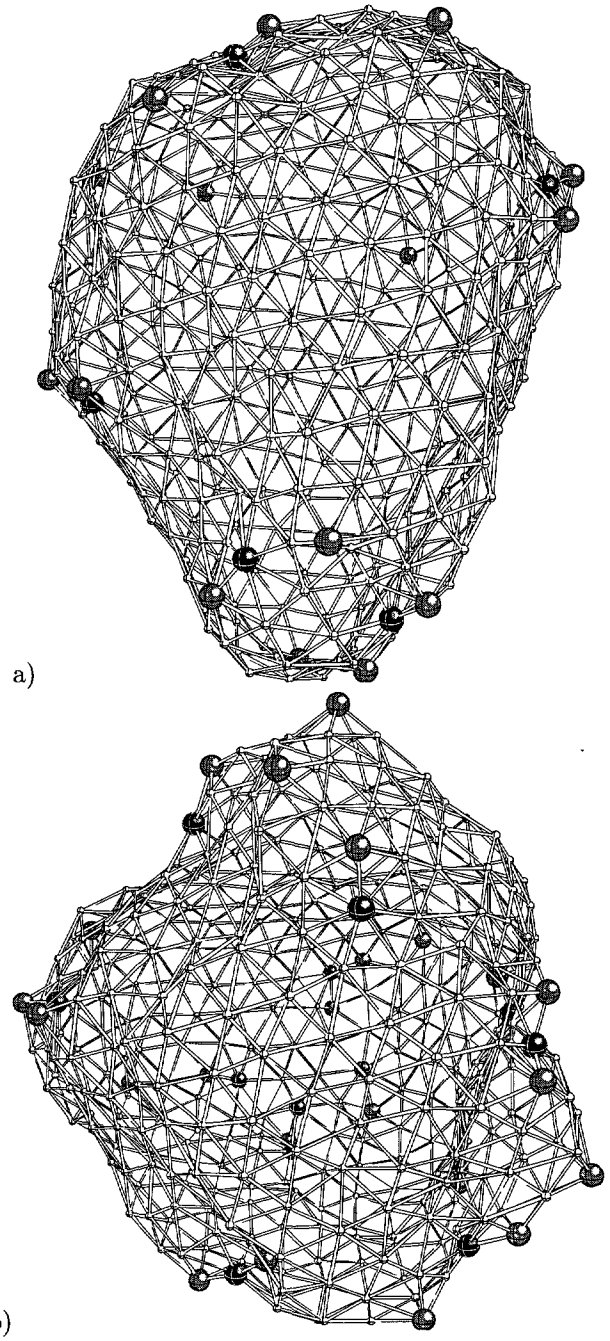

Fig. 7. — Vesicle shapes for a system of $N = 407$ beads, with $\lambda_b/T = 2.0$, and tether lengths (a) $\ell_0 = 1.330$, (b) $\ell_0 = 1.360$, and (c) $\ell_0 = 1.389$. Fivefold (sevenfold) disclinations are shown as large grey (black) spheres. Note that the sphere radius is unrelated to the radius of the beads in the simulation (which is identical for all beads).

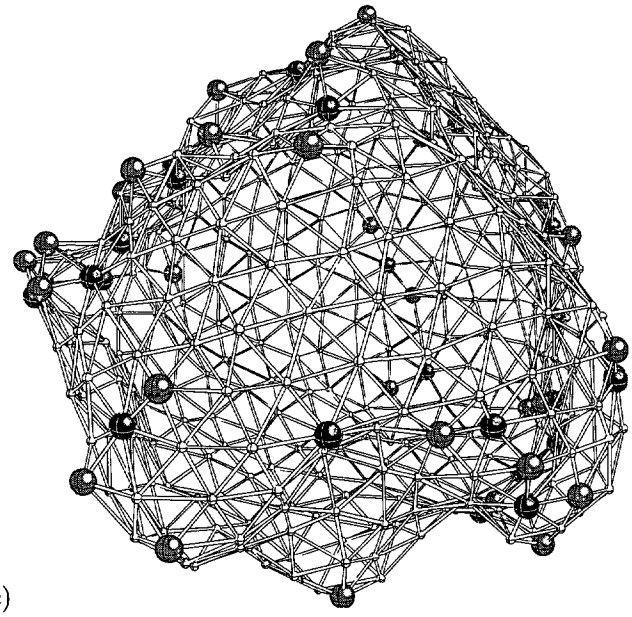

c)

Fig. 7. — *(Continued)*

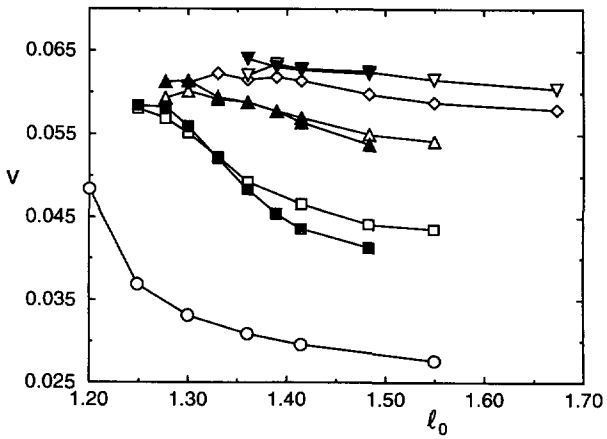

Fig. 8. — Scaled volume $v = \langle V \rangle N^{-3/2} \langle \ell \rangle^{-3}$, as a function of the tether length ℓ_0 (the symbols are the same as in Fig. 6).

slowly increase with decreasing tether length, while the peak widths slowly decrease. Thus, even for the smallest tether lengths studied, there are still pronounced shape fluctuations.

4.3. DEFECTS. — Typical defect configurations for $\lambda_b/T = 2.0$ and various tether lengths are shown in Figures 10. The configuration for the smallest tether length, $\ell_0 = 1.330$, shows that the number of dislocations is small, but that free dislocations are already present, in agreement with the result of reference [11]. The configuration for the largest tether length, $\ell_0 = 1.389$, demonstrates that the dislocation density is much larger, but free 7-fold disclinations are still

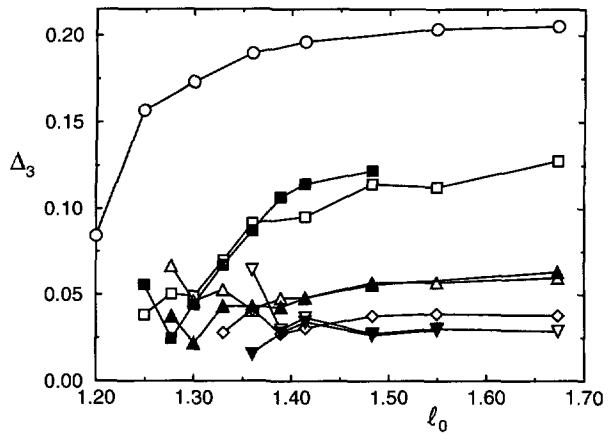

Fig. 9. — Asphericity Δ_3 as a function of the tether length ℓ_0 for various bending rigidities and system sizes (the symbols are the same as in Fig. 6).

rare. Finally, a comparison of Figures 10 with the defect configurations of a planar membrane, see Figures 3, indicates that the defect energy must be strongly reduced by buckling out of plane.

The defect configurations are characterized by averages of the number N_j of j-fold coordinates vertices, with $j \in [4, 5, 6, 7, 8]$. We identify a "free" dislocation with a 5/7-pair which has only sixfold coordinated vertices as nearest neighbors. Their number is denoted N_{dloc}. The quotation marks indicate that our definition of "free" dislocations includes both free disclinations as well as loosely bound dislocations pairs (with a minimum separation of two bond lengths). Note that not all free dislocations appear in N_{dloc}, because they might sit next to some other defect, like a dislocation pair. Similarly, a "free" five- or sevenfold disclination is identified with a five- or sevenfold coordinated vertex which has only sixfold coordinated neighbors. Their numbers are denoted $N_{5-\text{dclin}}$ and $N_{7-\text{dclin}}$.

The average densities of four-, six- and seven-fold coordinated vertices as a function of the tether length are shown in Figures 11. For the smallest tether lengths studied, the density $n_6 \equiv \langle N_6/(N-12)\rangle$ of 6-fold coordinated vertices approaches unity, see Figure 11a. The vesicles have a very small number of defects at these small tether lengths. For the largest tether lengths studied, n_6 is typically between 1/2 and 3/4. This corresponds to a high defect density, so that the membrane must certainly be in its fluid state. This picture is confirmed by the average number $n_7 \equiv \langle N_7/(N-12)\rangle$ of 7-fold coordinated vertices (see Fig. 11b): there are only a couple of these defects present for the smallest tether lengths. Note that the presence of a small number of 7-fold coordinated vertices is necessary to allow for diffusion within the membrane. The density n_7 increases roughly exponentially with increasing tether length, and begins to saturate at large tether lengths. The density n_4 of four-fold coordinated vertices (Fig. 11c) also increases roughly exponentially with ℓ_0, but is much smaller than n_7. Furthermore, it shows a very strong dependence on the bending rigidity: an increase of the bending rigidity from $\lambda_b/T = 1.5$ to $\lambda_b/T = 3.0$ decreases the density n_4 by two orders of magnitude. There are also pronounced finite-size effects: for small tether lengths (in the hexatic phase), all three defect densities decrease with increasing system size.

It is also interesting to study the average coordination number of the vertex with the largest number of nearest neighbors, $\langle q_{\max}\rangle$. This is shown in Figure 12. For the smallest tether

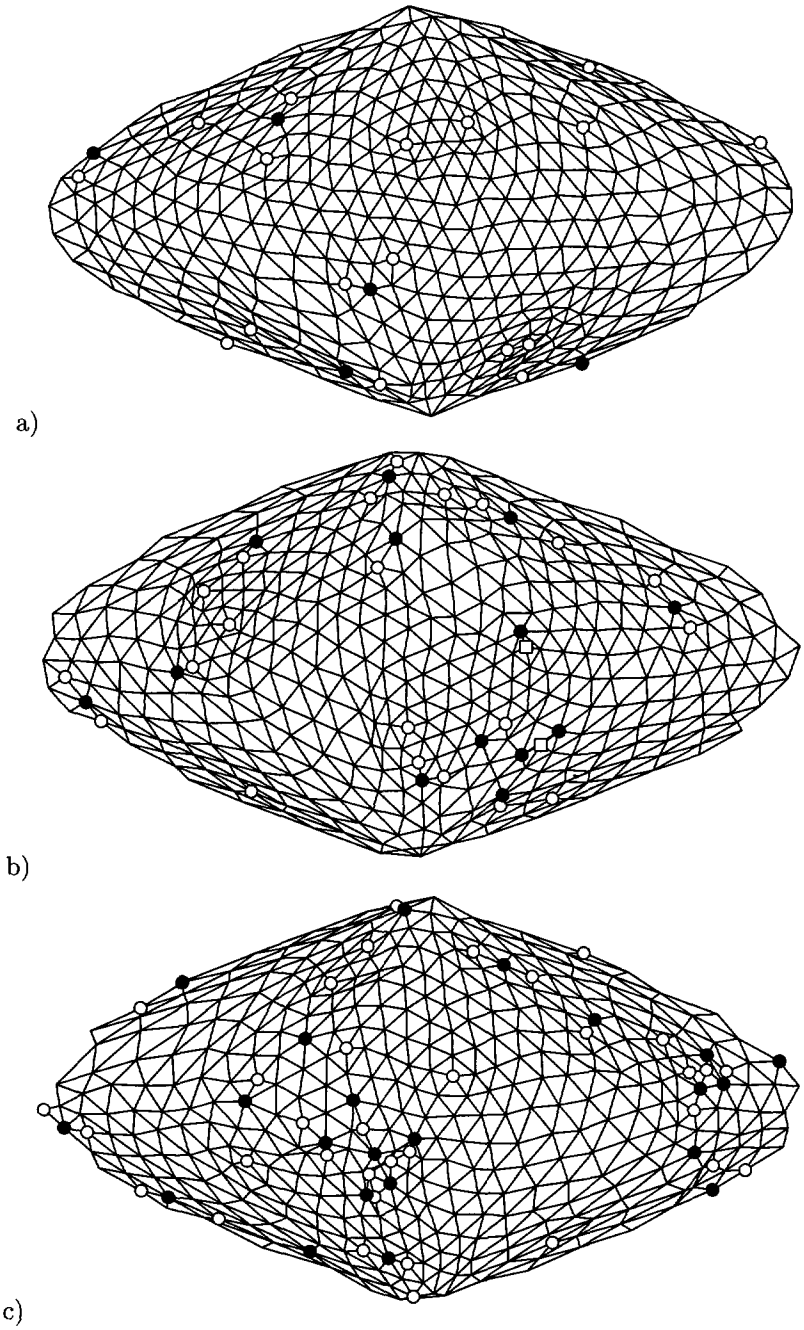

Fig. 10. — Distribution of topological defects on flexible vesicles (with $N = 407$) for bending rigidity $\lambda_b/T = 2.0$ and three different tether lengths, (a) $\ell_0 = 1.330$, (b) $\ell_0 = 1.360$, and (c) $\ell_0 = 1.389$. Fivefold (sevenfold) disclinations are shown by open (full) circles. The figure is a projection of the vesicle surface onto a plane; the projection of vertex i is given by $(\phi_i \sin(\theta_i), \theta_i)$, where ϕ_i and θ_i are the polar angles with respect to the vesicle's center of mass. The vesicle shapes of the same configurations are displayed in Figures 7.

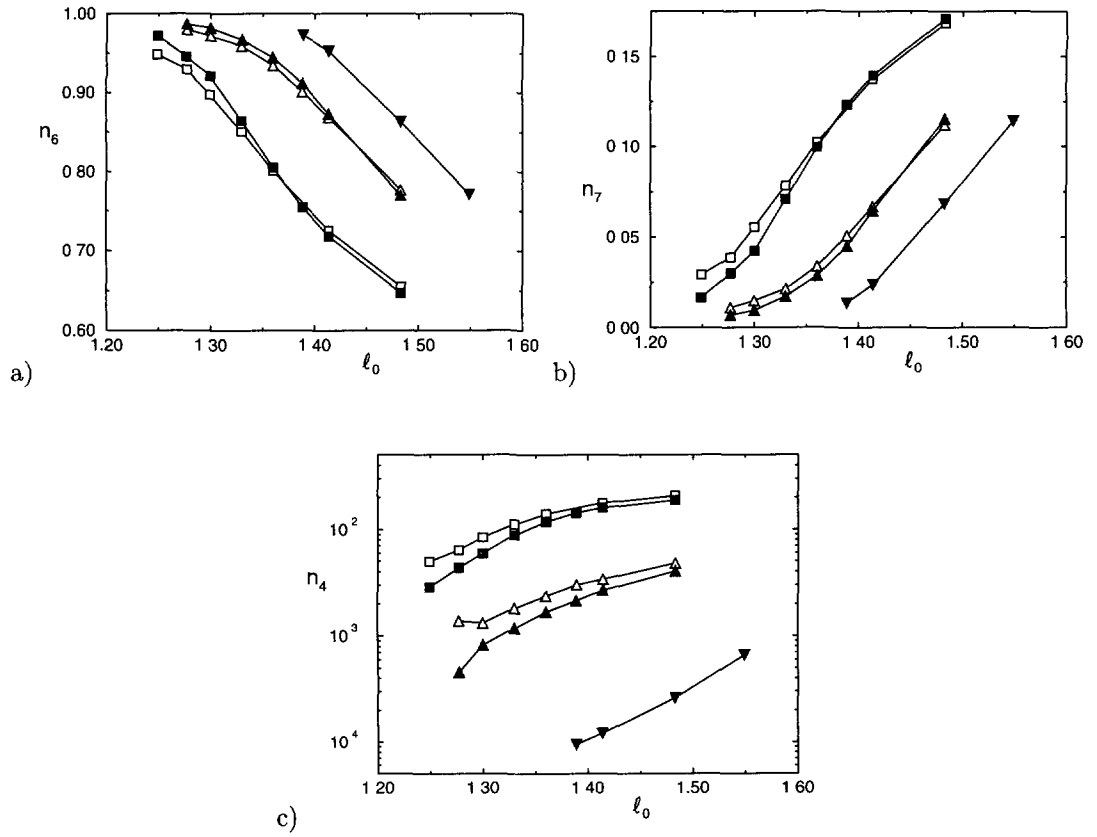

Fig. 11. — Densities $n_j = \langle N_j/(N-12)\rangle$ of j-fold coordinated vertices. (a) $j = 6$, (b) $j = 7$, and (c) $j = 4$. The symbols are the same as in Figure 6.

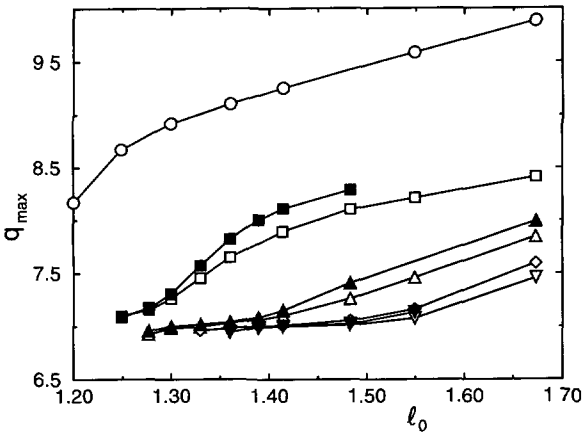

Fig. 12. — Average coordination number $\langle q_{max}\rangle$ of the vertex with the largest number of nearest neighbors as a function of the tether length ℓ_0 (the symbols are the same as in Fig. 6).

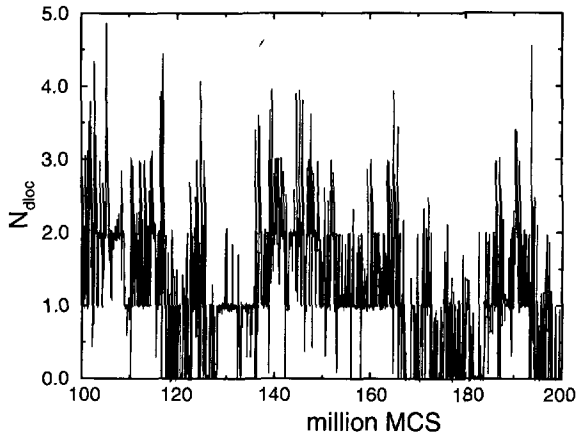

Fig. 13. — Number of "free" dislocations, N_{dloc}, averaged over 20 000 subsequent Monte Carlo steps, as a function of Monte Carlo time, for $N = 407$, $\lambda_{\mathrm{b}}/T = 2.0$ and $\ell_0 = 1.30$.

lengths studied, $\langle q_{\max} \rangle$ is slightly less than 7, which indicates that the membrane is occasionally completely free of defects. This can be seen explicitly by monitoring $q_{\max}$ as a function of Monte Carlo time. With increasing tether length, a plateau region is found where $\langle q_{\max} \rangle \simeq 7$. For larger tether lengths, $\langle q_{\max} \rangle$ increases again. The plateau region ends approximately at $\ell_0 \simeq 1.30$ for $\lambda_{\mathrm{b}}/T = 1.5$, $\ell_0 \simeq 1.40$ for $\lambda_{\mathrm{b}}/T = 2.0$, $\ell_0 \simeq 1.43$ for $\lambda_{\mathrm{b}}/T = 2.5$, and $\ell_0 \simeq 1.48$ for $\lambda_{\mathrm{b}}/T = 3.0$. No plateau regime is observed for $\lambda_{\mathrm{b}}/T = 1.0$.

4.4. Dislocations. — The number of "free" dislocations (averaged over 20 000 subsequent Monte Carlo steps) as a function of Monte Carlo time is shown in Figure 13 for $\lambda_{\mathrm{b}}/T = 2.0$ and $\ell_0 = 1.36$. The figure demonstrates that the (subaveraged) dislocation number fluctuates around some integer value over long time intervals, and then jumps to a new integer value as "free" dislocations form or recombine. This supports our conclusion that free dislocations are present at small values of the tether length.

The results of reference [11] suggest that the free energy of a free dislocation with Burgers vector $|\mathbf{b}| = \langle \ell \rangle$ should have the scaling form

$$\frac{1}{T} F_{\mathrm{disloc}} = \frac{\kappa}{T}\, \Theta\left(\frac{\kappa}{K_0 \langle \ell \rangle^2}\right), \tag{29}$$

if the system size is much larger than the buckling radius, $R_{\mathrm{b}} \simeq 127\kappa/(K_0\langle \ell \rangle)$, of a dislocation. For the parameter range studied in our simulations, we typically have $\kappa/(K_0\langle \ell \rangle^2) \leq 0.025$, which corresponds to the regime where defects easily buckle out of plane.

If the interaction between "free" dislocations is weak, the dislocation density, n_{dloc}, is therefore given by

$$\frac{T}{\kappa} \ln\left(n_{\mathrm{dloc}}\right) = -\,\Theta_{\mathrm{dloc}}\left(\frac{\kappa}{K_0 \langle \ell \rangle^2}\right). \tag{30}$$

Our Monte Carlo data for the dislocation density for various tether lengths (in the range $1.249 \leq \ell_0 \leq 1.483$) and bending rigidities λ_{b} are shown in the Figure 14. They confirm the scaling ansatz (30). Furthermore, the data are well fitted by a scaling function

$$\Theta_{\mathrm{dloc}}(x) = -2.25 \ln(15.6\, x). \tag{31}$$

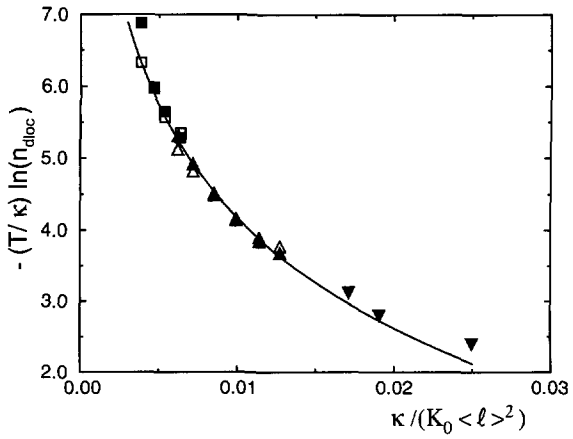

Fig. 14. — Scaling behavior of the density n_{dloc} of "free" dislocations for various bending rigidities, tether lengths, and systems sizes. Data are shown for $N = 247$ with $\lambda_b/T = 1.5$ (□), $\lambda_b/T = 2.0$ (△), and for $N = 407$ with $\lambda_b/T = 1.5$ (■), $\lambda_b/T = 2.0$ (▲), and $\lambda_b/T = 3.0$ (▼). The full line shows the approximation (31) for the scaling function $\Theta_{\mathrm{dloc}}(x)$.

This result indicates that the dislocation free energy might diverge in the inextensional limit $K_0 \to \infty$.

Finally, we want to compare our result (31) with the scaling function

$$\tilde{\Theta}_{\mathrm{dloc}}(x) = \frac{1}{8\pi}\frac{1}{x}\ln(127x) + c_{\mathrm{G}}, \tag{32}$$

where c_{G} is a constant, which was proposed by Seung and Nelson in reference [11]. The scaling function (32) is derived in the limit where the buckling radius is large compared to the lattice constant, *i.e.*, for $x \gg 1/127$. Nevertheless, for values of $c_{\mathrm{G}} \in [0, 1]$, the two expressions fit together reasonable well, with a crossover near $x \simeq 0.025$ (where $R_b/\langle\ell\rangle \simeq 3$); they should therefore be considered different limits of the same scaling function.

4.5. DISCLINATIONS. — The average number $\langle N_{5-\mathrm{dclin}}\rangle$ of "free" five-fold disclinations is shown in Figure 15. For a perfectly ordered system, $N_{5-\mathrm{dclin}} = 12$. With increasing tether length, $\langle N_{5-\mathrm{dclin}}\rangle$ decreases, because dislocations appear, some of which are attracted to the free 5-fold disclinations. This effect can be understood as a screening of the strain field near disclinations by free dislocations. Since $N_{5-\mathrm{dclin}}$ counts the number of five-fold coordinated vertices which have only 6-fold coordinated neighbors, disclination-dislocation pairs do not contribute. Although dislocations also begin to dissociate into weakly bound disclination pairs, this effect is apparently not strong enough to balance the screening effect.

The density of "free" 7-fold disclinations is shown in Figure 16. It shows the same sigmoidal shape as the other defect densities. The decrease of the density for $\lambda_b/T = 1.5$ for large tether lengths is again due to an over-crowding of defects, which does not leave enough space for "free" disclinations. A very remarkable property of $\langle n_{7-\mathrm{dclin}}\rangle$ are its finite-size effects: the density decreases with system size for small tether lengths, but increases for large tether lengths. The density curves for different system sizes therefore intersect; the point of intersection is located at $\ell_0 \simeq 1.315$ for $\lambda_b/T = 1.5$, and $\ell_0 \simeq 1.375$ for $\lambda_b/T = 2.0$. Note that the intersections almost coincide with the points of inflection of the curves.

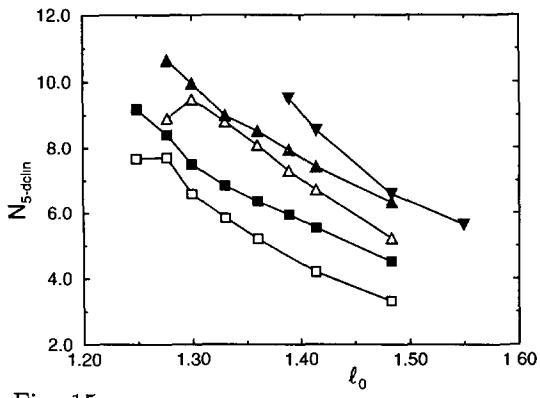

Fig. 15.

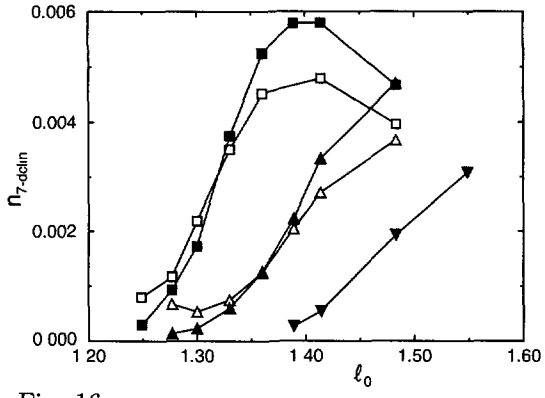

Fig. 16.

Fig. 15. — Average number $\langle N_{5-\mathrm{dclin}} \rangle$ of "free" five-fold disclinations as a function of the tether length ℓ_0 (the symbols are the same as in Fig. 14).

Fig. 16. — Average density $\langle n_{7-\mathrm{dclin}} \rangle$ of "free" seven-fold disclinations as a function of the tether length ℓ_0 (the symbols are the same as in Fig. 14).

The decrease of the density $\langle n_{7-\mathrm{dclin}} \rangle$ as a function of system size for small tether lengths (in the hexatic phase) is difficult to understand theoretically. In a hexatic phase, there should be no free disclinations in the thermodynamic limit, but only (weakly) bound pairs, which interact with a potential

$$V(r) = \alpha \ln(r/a), \tag{33}$$

where $a \simeq \langle \ell \rangle$ is a short-distance cutoff, and the amplitude α depends on both the bending rigidity λ_b/T and the tether length ℓ_0. In the hexatic phase, $\alpha/T > 4$. The density of loosely bound disclination pairs is then given by [48, 56]

$$n_{\mathrm{pairs}} = \mathrm{e}^{-2E_c/T} Z(\alpha), \tag{34}$$

where E_c is the core energy of a disclination, and

$$Z(\alpha) = \int_{r \geq r_{\min}}^{R} \frac{\mathrm{d}^2 r}{a^2} \exp[-V(r)/T] \tag{35}$$

$$= \frac{2\pi}{\alpha/T - 2} \left[(r_{\min}/a)^{-(\alpha/T-2)} - (R/a)^{-(\alpha/T-2)} \right], \tag{36}$$

where $r_{\min} \simeq 2a$ for our definition of "free" disclinations, and $R/a \sim \sqrt{N}$ is proportional to the linear system size. Strictly speaking, the integral in equation (35) has to be replaced by a sum over all possible distance vectors on the triangular lattice. Nevertheless, the result (36) indicates that the disclination density should exhibit only very weak finite size effects, and — more importantly in the present context — that the density should increase with increasing system size. The latter conclusion contradicts our Monte Carlo data.

The partition function (35) is dominated by closely bound disclination pairs. We have therefore tried to analyze our data for the density of "free" disclinations by assuming that most of the pairs we observe have a separation of just two bond lengths. In this case, their density should scale in exactly the same way as the dislocation density, equation (30), although with a different scaling function. However, the data do not scale very well in such a plot.

Finally, it has been argued recently by Park [57] that the finite-size effects on a fluctuating sphere are more complicated than for an almost planar membrane. Based on the analysis

of a sine-Gordon Hamiltonian [13] for membranes of arbitrary topology, he shows that for a fluctuating sphere the non-zero Gaussian curvature leads to a mass term proportional to $K_H/(\kappa R^2)$, where R is the vesicle radius [57]. The interaction between disclinations then follows the logarithmic behavior (33) only for length scales $r < r_D$, where $r_D = R\sqrt{\kappa/K_H}$, and decays exponentially for $r > r_D$. In the case where $\kappa/K_H \ll 1$, this leads to

$$Z(\alpha) \simeq \frac{2\pi}{\alpha/T-2}\left[(r_{min}/a)^{-(\alpha/T-2)} - (r_D/a)^{-(\alpha/T-2)}\right] + \pi(1-\kappa/K_H)(R/a)^2. \quad (37)$$

The dominant R-dependence is given by the second part of equation (37). The finite size effects are much more pronounced than in the case of a planar membrane. However, this model again predicts an increase of the density of "free" disclinations which system size, in contrast to the data presented in Figure 16. On the other hand, the broadening of the peak in the excess nearest-neighbor distance $\delta\ell$ with decreasing tether length, see Figure 6, could be an indication for a mass term as predicted by Park [57].

4.6. PHASE DIAGRAM. — Due to the complex quasi-spherical geometry and the relatively small system sizes we are able to simulate, we cannot hope to distinguish the fluid and hexatic phases by the asymptotic decay of the bond orientation correlation function. Instead, the internal order of the membrane has to be detected indirectly from its influence on the vesicle shapes and on the local defect numbers. We have already argued above that the transition is visible in $\langle V\rangle$ and the compressibility χ for a single system size. It should also show up in the scaling behavior of the compressibility with N [38]. In the hexatic phase, there should only be a weak N-dependence, while in the fluid phase, $\chi \sim N^\gamma$ with $\gamma \simeq 1.5$ [30]. The tether lengths at which the behavior of different observables changes markedly are summarized in Table I. From these numbers, we estimate that a phase transition occurs at $\ell_0 \simeq 1.10 \pm 0.10$ for $\lambda_b/T = 1.0$, $\ell_0 \simeq 1.31 \pm 0.04$ for $\lambda_b/T = 1.5$, $\ell_0 \simeq 1.37 \pm 0.04$ for $\lambda_b/T = 2.0$, and $\ell_0 \simeq 1.43 \pm 0.04$ for $\lambda_b/T = 3.0$. In fact, we cannot exclude the possibility that for $\lambda_b/T = 1.0$, a hexatic phase does not occur for any tether length. Thus, we find that decreasing the bending rigidity (at fixed tether length ℓ_0) leads to a transition from the hexatic to the fluid phase, in agreement with the predictions of references [12, 13]. In the limit $\lambda_b/T \to \infty$, we expect the transition to occur at the same tether length as for planar membranes, where our 2D simulation data are consistent with a fluid phase for $\ell_0 > 1.53 \pm 0.01$. The resulting phase diagram in the $T/(K_0\langle\ell\rangle^2) - T/\kappa$ plane is shown in Figure 17.

Because we have not been able to obtain good estimates for the hexatic stiffness, K_H, it is not possible to directly compare our phase diagram with theory. However, since K_H is a monotonic function of K_0 (for fixed κ/T), the general features are consistent with the predictions of

Table I. — *Estimates for the tether lengths ℓ_0 at the hexatic-fluid transition.*

λ_b/T	ω_{flip}	$\delta\ell$	q_{max}	v	χ	$n_{7-dclin}$
1.0				1.2		
1.5	1.33	1.30	1.30	1.33	1.33	1.315
2.0	1.41	1.36	1.40	1.36	1.38	1.375
2.5	1.55	1.39	1.43			
3.0	1.55	1.40	1.48	1.40	1.41	

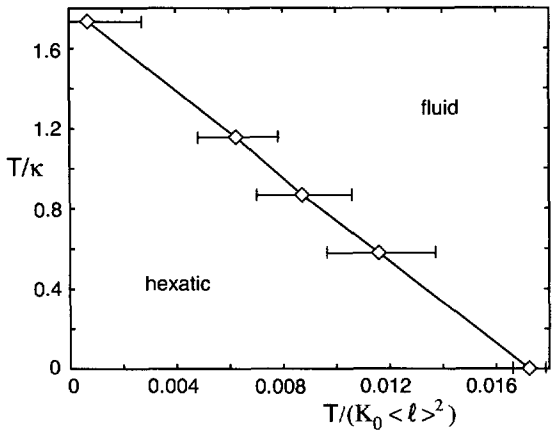

Fig. 17. — Phase diagram in the (T/κ)–$(T/(K_0\langle\ell\rangle^2))$-plane.

references [12, 13]. Our present data also do not allow us to characterize the transition in any detail or even distinguish between a true phase transition or a rapid crossover.

We want to remark parenthetically that the result of reference [18] — that the second term in equation (1) was able to regularize the internal geometry, but had little effect on the external geometry — can now be rather easily explained by the lack of a bending energy in the Hamiltonian, which implies that the membrane should remain fluid for all values of γ.

5. Summary and Discussion

In this paper we have investigated the properties of a simple tether-and-bead model of membranes and vesicles as a function of tether length and bending rigidity using Monte Carlo simulations and scaling arguments. For planar membranes, we find a first-order phase transition between a crystalline and a fluid phase at a tether length of $\ell_0 = 1.53 \pm 0.01$. This shows that the standard tether-and-bead model for flexible membranes can be used to study freezing. We have also determined the elastic constants — the area modulus K_A and the Young modulus K_0 — of the flat, crystalline phase, since they are needed for a detailed analysis of the behavior of flexible membranes.

For flexible vesicles, we give strong evidence for the presence of a hexatic phase for sufficiently small tether lengths, in agreement with the predictions of Seung and Nelson [11]. In particular, we show that the density of dislocations with Burgers vector $\langle\ell\rangle$ scales as a function of $\kappa/(K_0\langle\ell\rangle^2)$ in the hexatic phase. The position of the hexatic-to-fluid transition has been estimated for several values of the bending rigidity, as summarized in Table I. We find that the tether length at the transition decreases with decreasing bending rigidity, in qualitative agreement with the field-theoretic calculations of references [12, 13].

The results summarized above confirm the current theoretical understanding of the freezing of flexible vesicles. Our results for the finite-size behavior of the density of "free" disclinations, however, seems to be inconsistent with theory. Whereas current theories lead us to expect that the disclination density in the hexatic phase increases with increasing system size, the Monte Carlo data shows that it decreases. Similar finite-size behavior is also observed for the densities of four- and seven-fold-coordinated vertices.

There are a number of conceivable explanations for this discrepancy. The most obvious difficulty is our identification of "free" disclinations. Since only sevenfold-coordinated vertices

which have only sixfold-coordinated neighbors are counted as "free" disclinations, all disclinations which are adjacent to a free dislocation or some other defect are not taken into account in $\langle N_{\mathrm{dclin}} \rangle$. Thus, we certainly underestimate the number of weakly bound disclination pairs. It is less clear, however, how this will affect the finite-size behavior of $\langle N_{\mathrm{dclin}} \rangle$. Another possible explanation is on the theoretical side. The calculation of reference [57] is for a weakly fluctuating sphere. However, it has been shown in reference [15] — in qualitative agreement with our Monte Carlo results — that hexatic vesicles are not spherical, but have the shape of a smoothed-out icosahedron. There is therefore a non-uniform distribution of Gaussian curvature, which is not taken into account in the analysis of reference [57]. Again, it is difficult to estimate how this might affect the finite-size behavior of the disclination density.

On a quantitative level, several questions require further investigations. First, for a direct comparison of theory and simulations, the hexatic stiffness K_{H} has to be determined. This is a rather difficult task, which to our knowledge has not been attempted even for models of planar two-dimensional systems. Second, the finite-size effects in the hexatic phase have to be better understood. We are planning simulations for larger system sizes in the future in order to see if the finite-size behavior observed here is an artifact due to the relatively small system sizes studied. It is quite obvious, however, that systems with more than 1000 vertices cannot be simulated at present. Finally, it will be interesting to allow for out-of-plane fluctuations of (almost) planar membranes with periodic boundary conditions. The finite-size effects in this case are expected to be quite different from those of vesicles [57]; this would allow a more detailed comparison of simulations and current theories of freezing.

Acknowledgments

We thank D. Frenkel, M. Kraus, H. Löwen, T. Lubensky, and D. Nelson for helpful discussions. This work was supported in part by the National Science Foundation under Grant No. DMR-9405824, the donors of The Petroleum Research Fund, administered by the ACS, the U.S. Army, Army Research Laboratory, Army HPC Research Center, the Deutsche Forschungsgemeinschaft, and NATO grant CRG910156.

References

[1] Kosterlitz J.M. and Thouless D.J., *J. Phys.* C **6** (1973) 1181.
[2] Halperin B.I. and Nelson D.R., *Phys. Rev. Lett.* **41** (1978) 121.
[3] Nelson D.R. and Halperin B.I., *Phys. Rev.* B **19** (1979) 2457.
[4] Young A.P., *Phys. Rev. B* **19** (1979) 1855.
[5] Nelson D.R., in "Phase Transitions and Critical Phenomena", C.Domb and J. Lebowitz, Eds. (Academic Press, London, 1983), Vol. 7, pp. 1-99.
[6] Chui S.T., *Phys. Rev.* B **28** (1983) 178.
[7] Lipowsky R., *Nature* **349** (1991) 475.
[8] Nelson D.R., in "Fluctuating Geometries in Statistical Mechanics and Field Theory", F. David, P. Ginsparg and J. Zinn-Justin, Eds. (North-Holland, Amsterdam, 1996), pp. 423-477.
[9] Peliti L., in "Fluctuating Geometries in Statistical Mechanics and Field Theory", F. David, P. Ginsparg and J. Zinn-Justin, Eds. (North-Holland,Amsterdam, 1996), pp. 195-285.
[10] Nelson D.R. and Peliti L., *J. Phys. France* **48** (1987) 1085.
[11] Seung H.S. and Nelson D.R., *Phys. Rev.* A **38** (1988) 1005.
[12] Guitter E. and Kardar M., *Europhys. Lett.* **13** (1990) 441.
[13] Park J.-M. and Lubensky T.C., *Phys. Rev.* E **53** (1996) 2648.

[14] Lubensky T.C. and Prost J., *J. Phys. II France* **2** (1992) 371.
[15] Park J.-M., Lubensky T.C. and MacKintosh F.C., *Europhys. Lett.* **20** (1992) 279.
[16] Deem M.W. and Nelson D.R., *Phys. Rev.* E **53** (1996) 2551.
[17] Park J.-M. and Lubensky T.C., *J. Phys. I France* **6** (1996) 493.
[18] Baillie C.F. and Johnston D.A., *Phys. Rev.* D **48** (1993) 5025.
[19] Ferguson N. and Wheater J.F., *Phys. Lett.* B **319** (1993) 104.
[20] Billoire A. and David F., *Nucl. Phys.* B **275** (1986) 617.
[21] Boulatov D.V., Kazakov V.A., Kostov I.K. and Migdal A.A., *Nucl. Phys.* B **275** (1986) 641.
[22] Ho J.-S. and Baumgärtner A., *Europhys. Lett.* **12** (1990) 295.
[23] Kroll D.M. and Gompper G., *Science* **255** (1992) 968.
[24] Boal D.H. and Rao M., *Phys. Rev.* A **45** (1992) 6947.
[25] Gompper G. and Kroll D.M., *Europhys. Lett.* **19** (1992) 581.
[26] Kroll D.M. and Gompper G., *Phys. Rev.* A **46** (1992) 3119.
[27] Gompper G. and Kroll D.M., *Phys. Rev.* A **46** (1992) 7466.
[28] Dammann B., Fogeby H.C., Ipsen J.H. and Jeppesen C., *J. Phys. I France* **4** (1994) 1139.
[29] Gompper G. and Kroll D.M., *Phys. Rev. Lett.* **73** (1994) 2139.
[30] Gompper G. and Kroll D.M., *Phys. Rev.* E **51** (1995) 514.
[31] Ipsen J.H. and Jeppesen C., *J. Phys. I France* **5** (1995) 1563.
[32] Gompper G. and Kroll D.M., *J. Phys. I France* **6** (1996) 1305.
[33] Gompper G. and Kroll D.M., *Phys. Rev. Lett.* **71** (1993) 1111.
[34] Gompper G. and Kroll D.M., *Phys. Rev.* E **52** (1995) 4198.
[35] Nielsen M. *et al.*, *Phys. Rev.* E **54** (1996) 6889.
[36] Kumar P.B.S. and Rao M., *Phys. Rev. Lett.* **77** (1996) 1067; *Phys. Rev. Lett.* **79** (1997) 1169 (Reply).
[37] Lowe C.P., van Roij R. and Frenkel D., *Phys. Rev. Lett.* **79** (1997) 1168 (Comment).
[38] Gompper G. and Kroll D.M., *Phys. Rev. Lett.* **78** (1997) 2859.
[39] Kantor Y. and Nelson D.R., *Phys. Rev. Lett.* **58** (1987) 2774.
[40] McDonald I.R., *Mol. Phys.* **23** (1972) 41.
[41] Yashonath S. and Rao C.N.R., *Mol. Phys.* **54** (1985) 245.
[42] Allen M.P. and Tildesley D.J., Computer Simulation of Liquids (Clarendon Press, Oxford, 1992).
[43] David F., in "Statistical Mechanics of Membranes and Surfaces", D. Nelson, T. Piran and S. Weinberg, Eds. (World Scientific, Singapore, 1989), pp. 157-223.
[44] Parrinello M. and Rahman A., *Phys. Rev. Lett.* **45** (1980) 1196.
[45] Parrinello M. and Rahman A., *J. Appl. Phys.* **52** (1981) 7182.
[46] Boal D.H., Seifert U. and Shillcock J.C., *Phys. Rev.* E **48** (1993) 4274.
[47] Note that a factor s_1 is missing in equations (8, 9) of reference [46].
[48] Bladon P. and Frenkel D., preprint (1997).
[49] Zollweg J.A. and Chester G.V., *Phys. Rev.* B **46** (1992) 11186.
[50] Lee J. and Strandburg K.J., *Phys. Rev.* B **46** (1992) 11190.
[51] Weber H. and Marx D., *Europhys. Lett.* **27** (1994) 593.
[52] David F., Guitter E. and Peliti L., *J. Phys. France* **48** (1987) 2059.
[53] de Gennes P.-G. and Taupin C., *J. Phys. Chem.* **86** (1982) 2294.
[54] Peliti L. and Leibler S., *Phys. Rev. Lett.* **54** (1985) 1690.
[55] Helfrich W., *J. Phys. France* **46** (1985) 1263.
[56] Fisher D.S., Halperin B.I. and Morf R., *Phys. Rev.* B **20** (1979) 4692.
[57] Park J.-M., *Phys. Rev.* E **54** (1996) 5414.